

Compliant Motion Control of Wheel-Legged Humanoid Robot on Rough Terrains

Lingxuan Zhao , Zhangguo Yu , Member, IEEE, Lianqiang Han , Xuechao Chen , Member, IEEE,
Xuejian Qiu , and Qiang Huang , Fellow, IEEE

Abstract—Wheeled-legged humanoid robots combine the rough terrain compliance of humanoid robots with the high efficiency of wheeled robots, enabling the robot to achieve flexible and stable locomotion over multiple terrains. However, the stability control of the wheel-legged humanoid robot in dealing with rough terrains and unexpected external disturbances remains unsolved. In the current investigation, a compliant balance control framework (CBCF) is proposed, which can absorb ground shocks, withstand unexpected external disturbances, and remain stable posture during motion. The CBCF connects the control of legs movement and the wheels balance control through the movement of the robot's center of mass. The wheel balance control employs the inverted pendulum model and controls the two wheels through model prediction. The leg posture control utilizes a whole-body dynamic compensator to realize the compliant motion and remain a stable posture. Cooperating with the high-level motion planner, the CBCF can allow the BHR-WI to move quickly and perform excellent adaptation in unmodeled rough terrains, and it is able to appropriately handle unexpected external disturbances as well. It is also worth mentioning that the BHR-WI is capable of remaining balance and quickly recovering stability in the event of a disturbance, even if one of the legs leaves the ground. Finally, tests confirm that the BHR-WI could withstand sustained unexpected disturbances, could smoothly cross the grass and steps and even realize high maneuverability in jumping.

Index Terms—Compliant motion control, unexpected disturbances, unmodeled rough terrains, wheel-legged humanoid robot.

Manuscript received 13 August 2023; accepted 16 September 2023. Date of publication 13 October 2023; date of current version 18 June 2024. Recommended by Technical Editor S. Mohan and Senior Editor K. Oldham. This work was supported in part by the National Natural Science Foundation of China under Grant 62073041 and Grant 61973039, and in part by the "111" Project under Grant B08043. (Corresponding author: Zhangguo Yu.)

Lingxuan Zhao, Lianqiang Han, and Xuejian Qiu are with the School of Mechatronical Engineering, Beijing Institute of Technology, Beijing 100081, China, and also with the Key Laboratory of Biomimetic Robots and Systems, Ministry of Education, Beijing 100081, China (e-mail: zhaolx@bit.edu.cn; hanlianqiang@88.com; 3120200161@bit.edu.cn).

Zhangguo Yu, Xuechao Chen, and Qiang Huang are with the School of Mechatronical Engineering, Beijing Institute of Technology, Beijing 100081, China, and also with the National Key Lab of Autonomous Intelligent Unmanned Systems, Beijing 100081, China (e-mail: yuzg@bit.edu.cn; chenxuechao@bit.edu.cn; qhuang@bit.edu.cn).

This article has supplementary material provided by the authors and color versions of one or more figures available at <https://doi.org/10.1109/TMECH.2023.3320762>.

Digital Object Identifier 10.1109/TMECH.2023.3320762

I. INTRODUCTION

MOBILITY is one of the important characteristics of robots. Wheeled robots have the advantages of high efficiency and strong load, but also have the shortcomings of poor ability to absorb ground impact, withstand lateral disturbances, and overcome obstacles [1], [2], [3], [4], [5]. In general, the legged robots have the greatest potential to adapt to uneven terrain. In recent years, Gong et al. [6], [7] employed the feedback control for standing and walking using virtual constraints methods and gait libraries on Cassie to methodically comprehend walking on sidewalks, grass, and snow. The humanoid robot Atlas of Boston Dynamics can walk, run, and jump in an outdoor environment [8], demonstrating excellent compliance and adaptation in unfamiliar terrain. Sygulla and Rixen [9], [10] developed a ground force control scheme that enables the humanoid robot Lola to walk over a uneven terrain with a 6 cm variation in ground height at a walking speed of 0.5 m/s. Han et al. [11] proposed a variable step size adjustment and control approach based on virtual constraints and implemented a stable walking simulation of an underactuated bipedal robot on a random discrete terrain simulation. Wang et al. [12] designed a parallel quadrupedal robot that can estimate terrain parameters by fusing the body, leg, and contact information. On the basis of virtual model control (VMC) with the quadratic programming (QP) method, the robot can achieve perception-less terrain adaptation.

Although legged robots have made some progress in compliance and passability, the locomotion performance of legged robots is still not satisfactory. Combining the advantages of wheeled and legged robots is a promising solution. Chen et al. [13] established a framework for the bipedal robot Cassie to dynamically ride a pair of Hovershoes on various terrains. However, since the internal state of Hovershoes cannot be fed back to Cassie's controller, this causes Cassie to shake when facing continuous uneven terrains. In addition, many investigators have adopted the integrated design of wheeled and legged robots. The Handle of Boston Dynamic is an excellent electric and hydraulic hybrid-driven wheel-legged robot. The main task of Handle is to maintain body balance through the movement of the legs and trunk, and realize compliant movement on uneven terrain, such as walking on grass and going down steps. Further, such a robot is able to carry heavy objects and jump over obstacles [14], but a paper reference on this is not available. The hydraulic wheel-legged robot (WLR) is capable of traversing slightly rough terrains and carrying objects [15], but cannot

cope with rapid changes in terrain when the robot moves at high speed [16]. Ascento is a compact wheeled bipedal robot, which decouples stabilizing and jumping control through an optimized three bar linkage, so that the center of mass (CoM) trajectory of the robot is an approximate linear motion perpendicular to the ground when the robot bends its legs [17], [18]. The proposed sequential feed forward controller plans only the hip joint trajectories via a proportional-integral-derivative (PID) controller, which can generate jumping trajectories for Ascento that do not cause body rotation. However, this leg control method, which neglects the upper body posture control, faces challenges in its application to our BHR-WI, where multijoint coordinated control of the legs is necessary, and upper body control cannot be disregarded. Ollie is a wheel-legged robot composed of two planar parallel mechanism legs and a balancing tail ending with passive wheel [19]. The proposed control method uses the value iteration (VI) algorithm to train the initial controller offline and uses the policy iteration (PI) algorithm to update the adaptive optimal controller online to train the balance controller. By using the whole body control (WBC) with the balance controller, Ollie shows a good performance in the real experiments [20]. However, the proposed control method is trained without considering disturbances, which could pose challenges for the robot's motion on unmodeled rough terrains. Zhu et al. [21] proposed a reinforcement learning (RL)-based hierarchical control framework for path tracking of wheeled bipedal robot, which can achieve stable path tracking. However, they have not yet applied RL for motion on rough terrains. Utilizing the trajectory optimization framework [22], [23] and the reinforcement learning controller [24], the wheel-legged quadruped robot ANYmal shows a remarkable ability to drive wheels and traverse obstacles with legs. This robot could also employ two wheels to provide its balance and demonstrate some compliance.

Obviously, the wheel-legged humanoid robot exhibits strong robustness and high motion efficiency and has the potential for flexible movement on rough terrains. Although some progress has been made in the research of wheeled biped robots, the compliance and stability of adult-sized wheel-legged humanoid robots on rough terrains still need to be improved. As presented in Figs. 1 and 2(a), a novel electrically-driven wheel-legged humanoid robot (BHR-WI) [25] is designed by our research group. We employ BHR-WI for experimental research on robot motion control in unstructured environments, and it can resist external disturbances, crawl through low passages, transit from standing to crawling [26] and climb steps with arms and legs.

In the balance control of the wheels, many two-wheel-legged robots do not consider the influence of the independent motion of the two legs, which is unfavorable for the stability control. The leg posture control as well as the wheel balance control should be appropriately integrated, so that the robot exhibits excellent compliance and anti-disturbance. Herein, we propose a compliant balance control framework (CBCF) that can absorb shocks through leg motion and adjust wheel balance control in real-time based on the leg posture. It is worth mentioning that the proposed CBCF can also add the motion control of the arms to realize the expansion of multijoint cooperative control. The



Fig. 1. Wheel-legged humanoid robot BHR-WI. With the high-level motion planner and CBCF, BHR-WI can adapt to both indoor and outdoor terrains. The robot shown here is climbing slope, navigating through unknown grass, and descending multiple stairs.

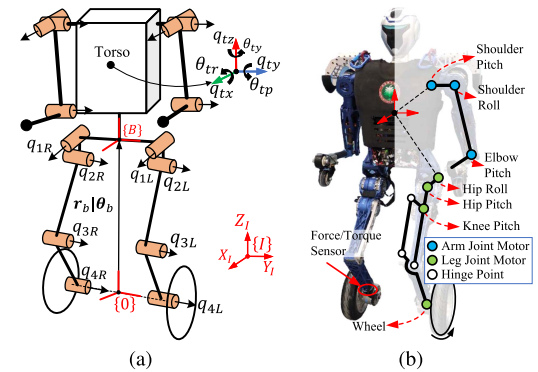


Fig. 2. (a) Mechanical structure and motor distribution of BHR-WI. (b) Kinematic model of BHR-WI. Frame $\{B\}$ is attached to the trunk. The origin of frame $\{0\}$ is located at the midpoint of the two wheels, and the positive direction of X_0 coincides with the forward direction of the robot.

performed tests in the manuscript reveal that the frame could enable the robot to withstand sustained disturbances, traverse rough terrains and steps, and even jump. The main contributions of the present investigation have been summarized as follows.

- 1) A CBCF based on multidimensional virtual force-compensated torque control and model-predicted wheel torque control is developed to control the body posture and balance of the robot. This frame enables the flexible and compliant movement of the robot on unmodeled rough terrains.
- 2) A new balance control strategy is proposed, which fully considers the influence of the independent motion of the legs on the balance control of the wheel. The wheel balance control is adjusted based on the leg posture and motion of CoM, which enhances the control accuracy and stability.
- 3) Multidimensional virtual force posture control is performed on the heavy trunk to make the trunk perform desired motions to maintain the stability of the robot.

In this manuscript, experiments are conducted to validate the stability and robustness of the compliant balance control framework. The rest of this article is organized as follows. Section II

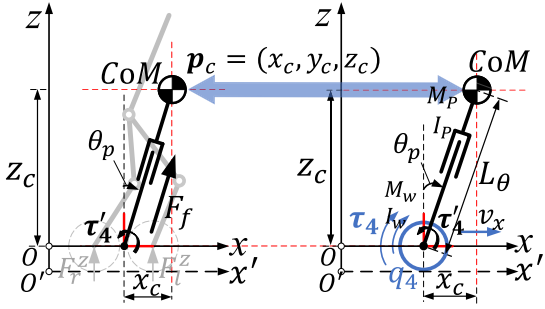


Fig. 3. Model decoupling. The two models are linked by the robot's CoM motion and the actual CoM is expressed as $p_c = (x_c, y_c, z_c)$.

provides the dynamic modeling process of BHR-WI. Section III describes the CBCF. In Section IV, related experiments reveal the compliance and robustness of our framework in dealing with unexpected disturbances and rough terrains. In Section V, some major conclusions and ideas for future work are provided.

II. MODELING OF WHEEL-LEGGED HUMANOID ROBOT

BHR-WI represents a complex wheel-legged system with complex dynamics (i.e., nonlinear and hybrid dynamics). We analyze the motion characteristics of the robot and adopt reduced-order models that are simpler and more intuitive to reflect the motion behavior. As illustrated in Fig. 3, we employ the linear inverted pendulum model (LIPM) to assess the basic dynamics of the humanoid robot, which can realize the CoM trajectory tracking and motion control of the humanoid robot [27], [28]. Further, the wheeled linear inverted pendulum model (W-LIPM) is utilized to complete the balance control of the wheeled robot [29].

Since LIPM exhibits an outstanding ability to reflect robot CoM behavior, W-LIPM should achieve accurate CoM information to get balance control. Therefore, we can closely combine these two models through robot CoM, whose coordinate is $p_c = (x_c, y_c, z_c)$.

A. Dynamic Model of Whole Body

Through the motion of legs, the robot can realize the compliant motion on rough terrains. We can generate leg joint torques based on the desired motion of the body relative to the wheels. As presented in Figs. 2(b) and 4(a), we define generalized coordinates, velocities, accelerations and torques in the frame $\{0\}$ as follows:

$$\begin{aligned}\mathbf{q} &= [r_b \ \theta_b \ q_{1L} \ \cdots \ q_{n_jL} \ q_{1R} \ \cdots \ q_{n_jR}]^T \\ \dot{\mathbf{q}} &= [\dot{r}_b \ \dot{\theta}_b \ \dot{q}_{1L} \ \cdots \ \dot{q}_{n_jL} \ \dot{q}_{1R} \ \cdots \ \dot{q}_{n_jR}]^T \\ \ddot{\mathbf{q}} &= [\ddot{r}_b \ \ddot{\theta}_b \ \ddot{q}_{1L} \ \cdots \ \ddot{q}_{n_jL} \ \ddot{q}_{1R} \ \cdots \ \ddot{q}_{n_jR}]^T \\ \boldsymbol{\tau} &= [\mathbf{0} \ \mathbf{0} \ \tau_{1L} \ \cdots \ \tau_{n_jL} \ \tau_{1R} \ \cdots \ \tau_{n_jR}]^T\end{aligned}$$

where $\mathbf{q}_b = [r_b, \theta_b]^T$ represents the virtual six DoFs of the floating base, including Cartesian coordinates of the trunk $r_b = [q_{tx}, q_{ty}, q_{tz}]^T$ and Euler angles $\theta_b = [\theta_{tr}, \theta_{tp}, \theta_{ty}]^T$ in

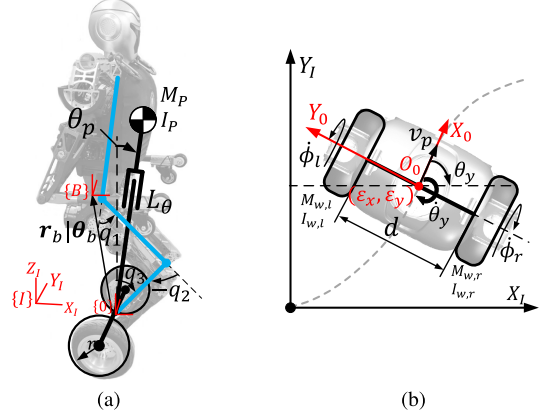


Fig. 4. (a) Wheeled linear inverted pendulum model with joints. (b) Wheeled linear inverted pendulum model under nonholonomic constraints. Define $\xi = [\varepsilon_x, \varepsilon_y, \theta_y, \theta_p, \phi_l, \phi_r]^T$ as the generalized coordinate of the model, which are all expressed in frame $\{I\}$. Temporarily, we do not consider the change of the robot's roll angle (θ_r).

X-Y-Z order. $\mathbf{q}_j = [q_{1L}, \dots, q_{n_jL}, q_{1R}, \dots, q_{n_jR}]^T$ is the generalized coordinate of the two legs, where $n_j = 4$. The factors q_1 , q_2 , and q_3 represent the hip roll, hip pitch, and knee pitch, respectively, and particularly q_4 denotes the rotation of the wheel. Due to the crucial significance of hip roll joints in bipedal walking, we have specifically incorporated them. Although they would not rotate during the motion in this manuscript, they will be utilized for achieving bipedal walking in the subsequent work on BHR-WI. The parameter $\boldsymbol{\tau}_a = [\tau_{1L}, \dots, \tau_{n_jL}, \tau_{1R}, \dots, \tau_{n_jR}]^T \in \mathbb{R}^{2n_j \times 1}$ represents the output torque of the actuated joints. The Euler parameters of the floating base θ_b are appropriately measured by the IMU installed within the robot's chest cavity. \mathbf{q}_j and $\dot{\mathbf{q}}_j$ are directly measured by the encoders mounted on the motors.

The floating-base dynamics equation can be derived using a standard Lagrangian formulation

$$\mathbf{M}(\mathbf{q})\ddot{\mathbf{q}} + \mathbf{H}(\mathbf{q}, \dot{\mathbf{q}})\dot{\mathbf{q}} + \mathbf{G}(\mathbf{q}) = \mathbf{S}_a^T \boldsymbol{\tau}_a + \mathbf{J}_e^T \mathbf{f}_e \quad (1)$$

where $\mathbf{M}(\mathbf{q}) \in \mathbb{R}^{(6+n) \times (6+n)}$ is the inertia matrix, $\mathbf{H}(\mathbf{q}, \dot{\mathbf{q}}) \in \mathbb{R}^{(6+n) \times (6+n)}$ is the centrifugal and Coriolis effects, $\mathbf{G}(\mathbf{q}) \in \mathbb{R}^{6+n}$ is generalized gravity vector, $\mathbf{S}_a = [\mathbf{0} \ \mathbf{I}_n] \in \mathbb{R}^{n \times (6+n)}$ is the selection matrix of actuated degrees of freedom, where $\mathbf{0}$ is zero matrix and \mathbf{I} is unit matrix. n is the total number of actuated joints. $\mathbf{f}_e = [\mathbf{f}_l^T, \mathbf{m}_l^T, \mathbf{f}_r^T, \mathbf{m}_r^T]^T$ is the combined contact forces (with force \mathbf{f} and moment \mathbf{m}) and $\mathbf{J}_e = [\mathbf{J}_l^T, \mathbf{J}_r^T]^T$ is a combined contact Jacobian.

B. Dynamic Model of Wheeled Linear Inverted Pendulum (W-LIPM)

To control the wheel, the BHR-WI is suitably reduced to a wheeled linear inverted pendulum model. We assume that the wheels undergo rolling in the forward direction without slipping. Also, the system is restrained by nonholonomic constraints, meaning no sliding along the direction perpendicular to the forward direction is allowed. The nonholonomic constraints

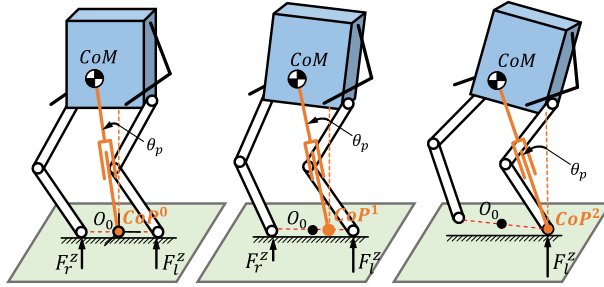


Fig. 5. CoP slides between two contact points, and when supported on a single leg, the CoP coincides with the contact point between the support wheel and the ground.

of BHR-WI can be described by $A(\xi)_{3 \times 6}\dot{\xi} = \mathbf{0}_{3 \times 1}$ [30], where $A(\xi)$ is the so-called Pfaffian matrix.

The dynamic equation of the system subject to nonholonomic constraints in standard form is

$$\begin{cases} M_w(\xi)\ddot{\xi} + H_w(\xi, \dot{\xi})\dot{\xi} + G_w(\xi) = S_w\tau_w + A^T(\xi)\lambda \\ \dot{A}(\xi)\dot{\xi} + A(\xi)\ddot{\xi} = 0 \end{cases} \quad (2)$$

where $M_w(\xi)$ is the inertia matrix, $H_w(\xi, \dot{\xi})$ is the centrifugal and Coriolis effects, $G_w(\xi)$ is the generalized gravity vector, $S_w \in \mathbb{R}^{6 \times 2}$ is input matching matrix, $\tau_w = [\tau_l, \tau_r]^T \in \mathbb{R}^{2 \times 1}$ is output torque vector, and λ is Lagrange Multipliers.

To calculate the driving torque of the wheel τ_w so that the robot can move with the desired acceleration $\dot{\xi}^d$, we define a new velocity vector $\nu = [v_p, \dot{\theta}_p, \dot{\theta}_y]^T$ [as presented in Fig. 4(b)], which satisfies $\dot{\xi} = F(\xi)\nu$, where $F(\xi) \in \mathbb{R}^{6 \times 3}$ is a linear operator that satisfies the relation: $A(\xi)F(\xi) = 0$.

Arrange the above equations and use the left multiplication $F^T(\xi)$, the dynamic equation of the system is obtained as

$$F^T M_w F \dot{\nu} + F^T (M_w \dot{F} \nu + H_w F \nu + G_w) = F^T S_w \tau_w. \quad (3)$$

Now, we know that the dynamic equation of the W-LIPM has two actuated torques $[\tau_l, \tau_r]^T$ and three degrees of freedom $[v_p, \dot{\theta}_p, \dot{\theta}_y]^T$, which is a second-order under-actuated system.

C. Calculation of CoP

The center of pressure (CoP) is the point where the force from the pressure field (normal to the sole) is applied and the resultant moment is zero [31], [32]. For bipedal robots, the CoP is the point inside the convex hull of the two contact areas. As the BHR-WI is in point contact with the ground, the convex hull of its contact area becomes a line connecting the two contact points (as presented by the red dotted line in Fig. 5).

When the robot is in the double support period, we can get the position of the CoP $p_{cop} = [x_{cop}, y_{cop}, z_{cop}]^T$ in frame {0}

$$\begin{cases} x_{cop} = (F_l^z x_{cop}^l + F_r^z x_{cop}^r)/(F_l^z + F_r^z) \\ y_{cop} = (F_l^z y_{cop}^l + F_r^z y_{cop}^r)/(F_l^z + F_r^z) \\ z_{cop} = 0 \end{cases} \quad (4)$$

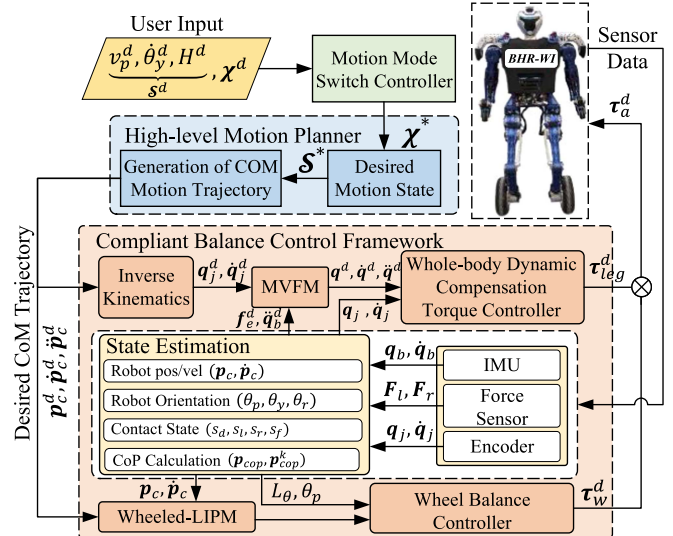


Fig. 6. Control diagram of compliant motion. The control frame requires user to input the desired motion mode χ^d and motion state S^d . The desired motion state S^d includes desired motion velocity v_p^d , desired rotation angular velocity $\dot{\theta}_y^d$, desired CoM height H^d . χ^* and S^* indicate the current motion mode and the desired motion state in the current mode, respectively. The superscript d indicates the desired value in the diagram.

where $p_{cop}^k = [x_{cop}^k, y_{cop}^k, z_{cop}^k]^T$, $(k = r, l)$ denotes the CoP position of two wheels in frame {0}, respectively. F_l^z and F_r^z are the vertical components of the forces at contact points p_{cop}^l and p_{cop}^r , which are measured by force/torque sensors [as shown in Fig. 2(a)].

In particular, when the robot is in the single-leg support period, the position of the CoP coincides with the contact point. When only the left leg is supported, $p_{cop} = p_{cop}^l$. Conversely, $p_{cop} = p_{cop}^r$.

III. COMPLIANT BALANCE CONTROL FRAMEWORK

Herein, we propose a compliant balance control framework that integrates the leg-compliant motion control and the fast wheel balance control through the robot CoM motion. As illustrated in Fig. 6, the control frame requires user to input the desired motion mode χ^d and motion state S^d . The desired motion mode χ^d includes jumping, crawling [26], walking, etc. According to the current motion mode χ^* and desired motion state S^* in the current mode, a high-level motion planner is employed to generate the desired CoM motion of the whole body. Then, the desired CoM motion will be simultaneously input to the whole-body dynamics compensation torque controller and wheel balance controller in CBCF to realize the coordination of leg motion and wheel balance. When the robot needs to move forward, the movement of the legs causes the CoM to shift forward, and the shift of the CoM makes the wheels generate forward acceleration and thus, move forward. The main algorithm of CBCF is present in Algorithm 1. In this section, the control method is described in some detail.

Algorithm 1: Main Algorithm of Compliant Balance Control Framework (CBCF).

Input: Desired CoM trajectory $\mathbf{p}_c^d, \dot{\mathbf{p}}_c^d, \ddot{\mathbf{p}}_c^d$
Output: Desired leg joint torque τ_{leg}^d and wheel torque $\tau_w^d = [\tau_l, \tau_r]^T$

```

1 /* Switch to CBCF when performing wheeled upright movement */ *
2 while Switch to CBCF do
3   Read current  $r_b, \dot{r}_b, \theta_b, \dot{\theta}_b, q_j, \dot{q}_j$  and  $\mathbf{F}_r, \mathbf{F}_l$  from sensors;
4   Update the real state of BHR-WI with state estimation;
5   /* Fast Wheel Balance Controller */ *
6   if  $\mathbf{F}_r = \mathbf{F}_l = \mathbf{0}$  then
7     |  $\tau_l = \tau_r = 0$ ; /* Flight phase */
8   else
9     | Update the values of  $L_\theta$  and  $\theta_p$  with  $\mathbf{p}_c$ ;
10    | Calculate the control variable  $\tau_w^d$  according to Eq.(15) and Eq.(16);
11    | if  $\mathbf{F}_r = 0$  or  $\mathbf{F}_l = 0$  then
12      | | Get  $\tau_l$ , and  $\tau_r = 0$  or get  $\tau_r$ , and  $\tau_l = 0$ ; /* Single-leg support */
13    | | else
14      | | Get  $\tau_l$  and  $\tau_r$ ; /* Double-leg support */
15    | end
16  end
17  /* Whole-body Dynamic Compensation Torque Controller */ *
18  Calculate  $\mathbf{q}_j^d$  and  $\dot{\mathbf{q}}_j^d$  by inverse kinematics using  $\mathbf{p}_c^d, \dot{\mathbf{p}}_c^d, \ddot{\mathbf{p}}_c^d$ ;
19  Get the desired acceleration  $\ddot{\theta}_{tp}^d$  and  $\ddot{\theta}_{tr}^d$  of trunk according to Eq.(5);
20  Get the total desired ground contact force  $\mathbf{f}_G^d$  according to Eq.(6);
21  Solve the optimization problem according to Eq.(9) to get  $\mathbf{f}_l^d$  and  $\mathbf{f}_r^d$ ;
22  Get the leg joint torque  $\tau_{leg}^d$  according to Eq.(11) and Eq.(12);
23 end
24 return  $\tau_{leg}^d$  and  $\tau_w^d$ ;

```

A. Dynamic Compensation Torque Control of Multidimensional Virtual Force

We design an inverse dynamic controller with multidimensional virtual force feedback to obtain the joint torques, and integrate the control of body posture and joint angle. The controller is capable of realizing the desired CoM trajectory of BHR-WI through controlling each joint. The specific algorithm is as follows:

1) Multidimensional Virtual Force for Trunk Posture Control:

The trunk posture control is of specific significance to control wheel balance and leg movement. We generate virtual torques by adjusting the spring-damper model and then, realize the control of the trunk through the torques of the hip joints. When the actual angle and the angular velocity of the trunk deviate forward from the desired angle and angular velocity, it is necessary to generate an optimal backward acceleration to compensate for the offset. On the contrary, a favorable forward acceleration should be created. As demonstrated in Fig. 7(a), the desired acceleration of the pitch and roll angles can be generated by

$$\begin{bmatrix} \ddot{\theta}_{tp}^d \\ \ddot{\theta}_{tr}^d \end{bmatrix} = \mathbf{K}_p^\theta \begin{bmatrix} \theta_{tp}^d - \theta_{tp} \\ \theta_{tr}^d - \theta_{tr} \end{bmatrix} + \mathbf{K}_d^\theta \begin{bmatrix} \dot{\theta}_{tp}^d - \dot{\theta}_{tp} \\ \dot{\theta}_{tr}^d - \dot{\theta}_{tr} \end{bmatrix} \quad (5)$$

where $\mathbf{K}_p^\theta = diag(k_p^{\theta 1}, k_p^{\theta 2})$ and $\mathbf{K}_d^\theta = diag(k_d^{\theta 1}, k_d^{\theta 2})$ are the proportional and differential gain diagonal matrices, θ and $\dot{\theta}$ are the actual trunk angle and angular velocity, d in the upper right corner specifies the desired value of the variable. The reference

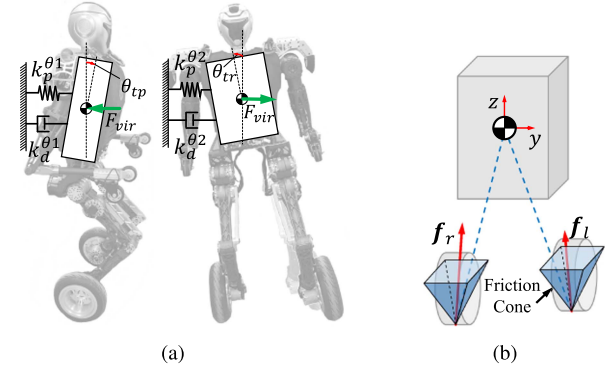


Fig. 7. (a) Virtual forces due to angular and angular velocity offsets.
(b) Friction constraints at contact points.

angular acceleration of the trunk output by the proportional-derivative(PD) controller forms a complete reference state with the expected angle of each leg joint.

2) Distribution and Optimization of the External Contact Force:

In order to control the torque of the whole body and to calculate the desired torque τ_a^d of each joint based on (1), we must give the desired external contact force \mathbf{f}_e^d . Since the point of contact of BHR-WI is with the ground, we can simplify the desired contact force as: $\mathbf{f}_e^d = [\mathbf{f}_l^{dT}, \mathbf{0}^T, \mathbf{f}_r^{dT}, \mathbf{0}^T]^T$.

In balance and body posture control, we should bring the ground contact force \mathbf{f}_G to a desired value \mathbf{f}_G^d for performing the desired task. For the availability of the force distribution, the relationship between \mathbf{f}_G^d and the contact forces should satisfy

the following relation: $\mathbf{f}_G^d = \mathbf{f}_l^d + \mathbf{f}_r^d$. Therefore, \mathbf{f}_G^d could be provided according to the desired task while compensating for gravity by

$$\ddot{\mathbf{f}}_G^d = M\mathbf{g} + M\ddot{\mathbf{p}}_c^d \quad (6)$$

where M is the total mass of the robot, \mathbf{g} is the gravity vector, and $\ddot{\mathbf{p}}_c^d$ is the desired acceleration of the desired task, which can be generated by

$$\ddot{\mathbf{p}}_c^d = \mathbf{K}_P^f(\mathbf{p}_c^d - \mathbf{p}_c) + \mathbf{K}_D^f(\dot{\mathbf{p}}_c^d - \dot{\mathbf{p}}_c) \quad (7)$$

where $\mathbf{K}_P^f = \text{diag}(k_p^{f1}, k_p^{f2}, k_p^{f3})$ is the proportional and $\mathbf{K}_D^f = \text{diag}(k_d^{f1}, k_d^{f2}, k_d^{f3})$ is the differential gain diagonal matrices, \mathbf{p}_c and $\dot{\mathbf{p}}_c$ are the position and velocity of the CoM.

Besides, to avoid contact point slip per the illustration given in Fig. 7(b), the contact force of each contact point must be in the following set:

$$\mathcal{K}_k = \left\{ \mathbf{f}_k \in \mathbb{R}^3 \mid \left| \frac{\sqrt{(f_k^x)^2 + (f_k^y)^2}}{f_k^z} \right| \leq \mu_f, f_k^z \geq 0 \right\} \quad (8)$$

where \mathcal{K}_k specifies a friction cone with an axis along the normal direction of the contact surface, and $k = l, r$.

Improving the stability and antidisturbance ability of the robot in multiple directions requires the correct distribution of end forces exerted on each leg. To achieve this goal, the error value between the actual CoP and the desired CoP of the robot should be appropriately minimized. During wheeled movement, we expect the robot to maintain an upright posture and be symmetrical about the sagittal plane, so the desired CoP is set to be located at the midpoint of the line connecting the two wheels. The optimization problem of the total end contact force distribution can be stated by

$$\begin{aligned} \min_{\mathbf{f}_l, \mathbf{f}_r} J &= \omega_1 \|(\mathbf{p}_{cop}^l - \mathbf{p}_{cop}) \times \mathbf{f}_l + (\mathbf{p}_{cop}^r - \mathbf{p}_{cop}) \times \mathbf{f}_r\|^2 \\ &\quad + \omega_2 \|\mathbf{f}_l\|^2 + \omega_3 \|\mathbf{f}_r\|^2 \end{aligned} \quad (9)$$

where ω_1, ω_2 , and ω_3 are the weights of objectives.

When optimizing the desired end contact force, we determine the weights by conducting multiple experiments and comparing the experimental results. A small value of weight ω_1 will cause the legs to bend more obviously during the movement. In the experiment, the robot will perform obvious tilt and shake when faced with force disturbance and rough terrain. Through the comparison of multiple experimental results, we finally set $\omega_1 = 10$ and $\omega_2 = \omega_3 = 0.02$.

3) Torque Control Based on Inverse Dynamic Compensation: To ensure the real-time performance of the whole model, a semifeedback inverse dynamic control is proposed, which would be capable of guaranteeing the normal operation of the multidegree-of-freedom dynamic solution process in the real-time program without optimization of the whole-body dynamics.

The movement of the CoM relative to the wheels is crucial for body posture control and wheel balance control. Based on trajectory planning or high-level instructions, we can generate the desired trajectory of the CoM in frame $\{0\}$ and use it to construct the desired state variables \mathbf{q}^d and $\dot{\mathbf{q}}^d$. When the robot

remains upright, we set the desired floating base translational position according to the desired CoM position, and set the desired translational velocity to zero.

As for the desired acceleration $\ddot{\mathbf{q}}^d$ required for inverse dynamics, only the desired angular acceleration of the floating base $\ddot{\theta}_b^d$ is nonzero. The desired angular acceleration of the leg joints is considered as $\ddot{\theta}_j^d = \mathbf{0}$.

Finally, we can obtain the desired acceleration of the robot's motion state variable as

$$\ddot{\mathbf{q}}^d = [\mathbf{0}_{3 \times 1} \quad \ddot{\theta}_{tp}^d \quad \ddot{\theta}_{tr}^d \quad 0 \quad \mathbf{0}_{n \times 1}]^T. \quad (10)$$

The feed-forward torque of each joint can be obtained as

$$\tau_{leg}^{ff} = S_a(M^d \ddot{\mathbf{q}}^d + \mathbf{H}^d \dot{\mathbf{q}}^d + \mathbf{G}^d - \mathbf{J}_e^T \mathbf{f}_e^d). \quad (11)$$

Due to the error of the dynamic model and the inaccuracy of joint motion, it is necessary to introduce the feedback compensation torque based on the feed-forward torque

$$\tau_{leg}^d = \tau_{leg}^{ff} + \underbrace{\mathbf{K}_p^\tau(\mathbf{q}_j^d - \mathbf{q}_j) + \mathbf{K}_d^\tau(\dot{\mathbf{q}}_j^d - \dot{\mathbf{q}}_j)}_{\tau_{leg}^c} \quad (12)$$

where \mathbf{K}_p^τ and \mathbf{K}_d^τ are the proportional and differential gain diagonal matrices. τ_{leg}^c is the compensation torque calculated by the PD feedback law.

B. Fast Wheel Balance Control

In previous experiments, we found that the general wheel balance control is more suitable for the robots with two wheels solidly connected and both moving on the ground. When the wheel-legged robot moves on rough terrain or is disturbed, this control cannot cope with the situation of loss contact with the ground, resulting in a loss of stability.

In the fast wheel balance control, we propose a novel approach: As illustrated in Fig. 5, we calculate the motion information of the CoM relative to the CoP and exploit it for balance control based on the model prediction. This approach considers the effect of contact state and leg posture on wheel balance, and allows to obtain a more accurate robot state for control. It can appropriately deal with the situation where the robot sways or the single leg of the robot leaves the ground during the motion, and substantially improve the robot's stability. We can get the position coordinates ${}^c\mathbf{p}_c$ of the robot's CoM relative to the CoP by ${}^c\mathbf{p}_c = \mathbf{p}_c - \mathbf{p}_{cop}$. Using ${}^c\mathbf{p}_c$, we can calculate the pendulum length L_θ and the actual inclination angle θ_p of the inverted pendulum model through the geometric relationship.

In the balance control of the WIPM, we choose $\mathbf{x} = [\theta_p, \theta_y, v_p, \dot{\theta}_p, \dot{\theta}_y]^T$ as the system's state vector. Near the equilibrium point, we can obtain the linear state-space equation of the system by approximate linearization. It is worth noting that the motion of the legs causes L_θ to change, and the state matrix \mathbf{A} and input matrix \mathbf{B} of the robot will change as L_θ changes. The state-space equation of the system can be given by

$$\dot{\mathbf{x}}(t) = \mathbf{A}(t)\mathbf{x}(t) + \mathbf{B}(t)\mathbf{u}(t) \quad (13)$$

where $\mathbf{u} = \tau_w = [\tau_l, \tau_r]^T$. In order to achieve more accurate balance control, we update matrix \mathbf{A} and \mathbf{B} in each control cycle.

MPC is a feedback control method that uses the current state value and target value of the state variable to predict and optimize the system response in advance. In order to facilitate the solution, it is necessary to discretize the state equation. We take the sampling time as Δt , then the discrete state variable satisfies $\mathbf{x}(k+1) = \mathbf{x}(k) + \dot{\mathbf{x}}(k) \cdot \Delta t$. We can adequately describe the system by a discrete-time state-space model

$$\mathbf{x}(k+1) = \overline{\mathbf{A}}(k)\mathbf{x}(k) + \overline{\mathbf{B}}(k)\mathbf{u}(k) \quad (14)$$

where $\overline{\mathbf{A}}(k) = \mathbf{I} + \Delta t \mathbf{A}(k)$, $\overline{\mathbf{B}}(k) = \Delta t \mathbf{B}(k)$, $\mathbf{x}(k)$, and $\mathbf{u}(k)$ represent the current state and the control input of the system, respectively. Equation (14) maps the current state $\mathbf{x}(k)$ and control input $\mathbf{u}(k)$ to the next state $\mathbf{x}(k+1)$.

Denote by $\mathbf{X}_k = \{\mathbf{x}(k), \mathbf{x}(k+1), \dots, \mathbf{x}(k+N)\}$ the predicted state trajectory in the predicted period, where $\mathbf{x}(k)$ is the current state at sampling time t_k and the following $\mathbf{x}(k+1), \dots, \mathbf{x}(k+N)$ are obtained according to (14), N is the prediction horizon.

In order to obtain the optimal control quantity $\mathbf{U}_k = \{\mathbf{u}(k), \mathbf{u}(k+1), \dots, \mathbf{u}(k+N-1)\}$, we define the cost function as

$$J = \sum_{i=0}^N \|\mathbf{x}(k+i) - \mathbf{x}_r(k+i)\|_Q^2 + \sum_{j=0}^{N-1} \|\mathbf{u}(k+j)\|_R^2 \quad (15)$$

where \mathbf{Q} and \mathbf{R} are the penalty matrices of the system motion state and control input, and $\mathbf{x}_r(t)$ represents the reference state trajectory.

During the operation of the inverted pendulum system, it should still be constrained by the physical world. Therefore, the solution of model predictive control is transformed into a quadratic programming problem

$$\begin{aligned} & \min_{\mathbf{U}_k} J \\ \text{s.t. } & \begin{cases} \mathbf{x}_{\min} \leq \mathbf{x}(k) \leq \mathbf{x}_{\max} \\ \mathbf{u}_{\min} \leq \mathbf{u}(k) \leq \mathbf{u}_{\max}. \end{cases} \end{aligned} \quad (16)$$

Now, the desired control input $\mathbf{u}(k)$ at the current moment can be obtained, and $\mathbf{u}(k)$ is the torque τ_w^d used to control the wheel balance. It is worth mentioning that in the balance control, only the condition where the wheels are in contact with the ground is taken into account, and when the wheel leaves the ground, the balance controller turns OFF. The switching of the balance controller is completed quickly within 1 ms without affecting the system's stability. The contact state between the wheel and the ground is determined by the contact forces \mathbf{F}_l and \mathbf{F}_r , and the contact state can be divided into double-leg support (s_d), single-leg support (s_l or s_r), and flight phase (s_f).

IV. EXPERIMENTS AND RESULTS

To validate the effectiveness and robustness of the CBCF, we conduct experiments on BHR-WI. The BHR-WI main electrical system consists of a computer, fourteen joint modules, two force/torque sensors, and an IMU [25]. For details, see the Appendix. By applying random disturbances, driving the robot on uneven grass, descending steps, and taking off and landing, we proved the coordination and unity of the leg compliant

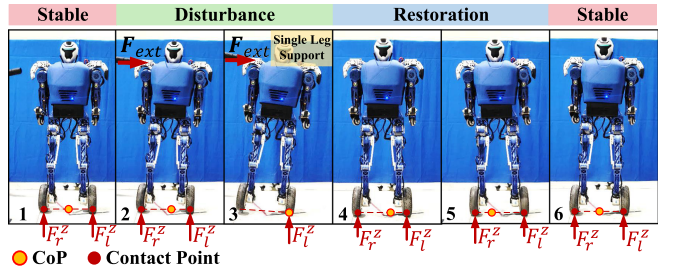


Fig. 8. Continuous lateral disturbances \mathbf{F}_{ext} cause the robot to leave the ground with one wheel, enter the single leg support period, and maintain stability. After removing the disturbing force, the robot restores the stability.

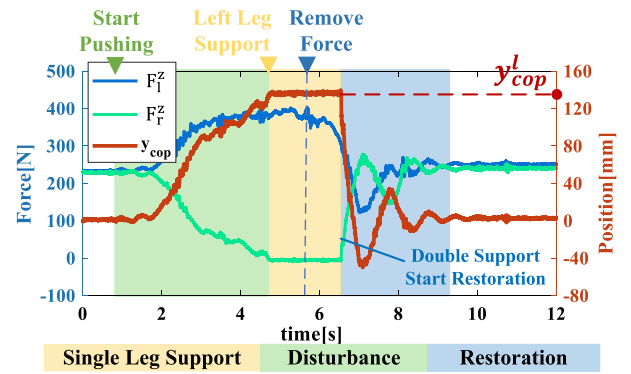


Fig. 9. Variations of the actual end forces and the CoP position during disturbance and recovery. The white background indicates the steady state, the green shaded area exhibits the continuous lateral disturbance, the yellow signifies the single leg support period after the disturbance, and the blue represents the posture recovery period after the disturbance is removed.

motion and fast wheel balance in CBCF. When conducting the experiments, we choose rough surfaces to prevent BHR-WI from losing stability due to slipping. The conducted experiments have proven that when faced with rough terrains, the BHR-WI would be capable of absorbing ground impact and rapidly restoring a stable state, which exhibits excellent compliance.

A. Random Disturbance Experiment

When the robot moves in the real environment, the disturbance force it receives enters from any direction and is applied to any position of the robot. Fig. 8 demonstrates the performance of the CBCF on posture control and disturbance resistance when lateral forces are applied, and such a plotted result in Fig. 9 properly exhibits the relationship between the CoP position and the ground reaction force. In the present experiment, the robot's shoulder is subjected to sustained lateral force, and a wheel is lifted off the ground. When the force/torque sensor detects that the wheel leaves the ground, the wheel will stop outputting torque and stop rotating, and the flying leg is held in the desired position by leg posture control. Then, the desired contact force of the supporting leg is increased to resist the camber torque caused by the disturbances. The CBCF can prevent the robot from falling. We see that the CoP position moves from the initial midpoint between the two wheels to the contact point between

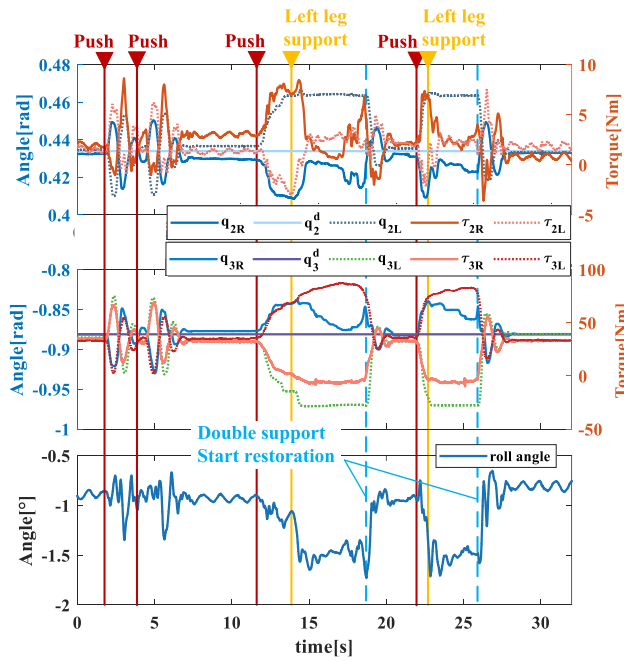


Fig. 10. Angles and torques of the hip and knee joints of two legs during the application of multiple random lateral disturbances. The red lines illustrate the moments when the lateral disturbance is applied. After being disturbed, the joint angle can quickly follow the desired value again to ensure the accuracy of posture.



Fig. 11. Stable movement of BHR-WI on the outdoor rough grassland.

the supporting wheel and the ground (the y -coordinate of contact point is denoted by y_{cop}^l). In this process, as long as the projection of the CoM on the ground does not cross the support point, the robot can restore the double-leg support and wheel balance under the action of gravity and inertia when the lateral disturbance is removed.

In addition, we applied multiple randomly lateral disturbance forces. The first two times will not make the wheels leave the ground, whereas the second two times will cause the robot to enter the single leg support state. Fig. 10 illustrates the angles and output torques of the hip and knee joints of two legs in the presence of the disturbance conditions. In the case of multiple lateral disturbances, the joint output torque changes with the joint angle, thus resisting the posture changes caused by the disturbance.

Also, as shown in Fig. 11, the BHR-WI can achieve a stable movement of 7.6 km/h on the unknown rough grassland with a load of 3.0 kg. During motion, BHR-WI goes through many short

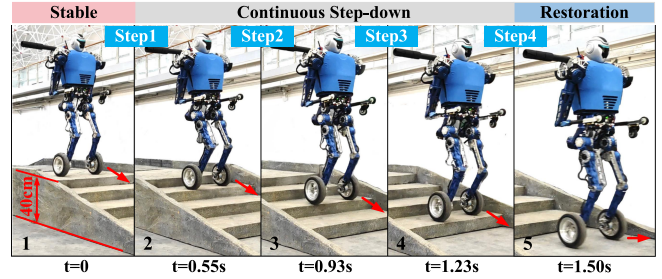


Fig. 12. BHR-WI is placed at the top of a step 40 cm high (10 cm per step) and reaches the ground in 1.5 s.

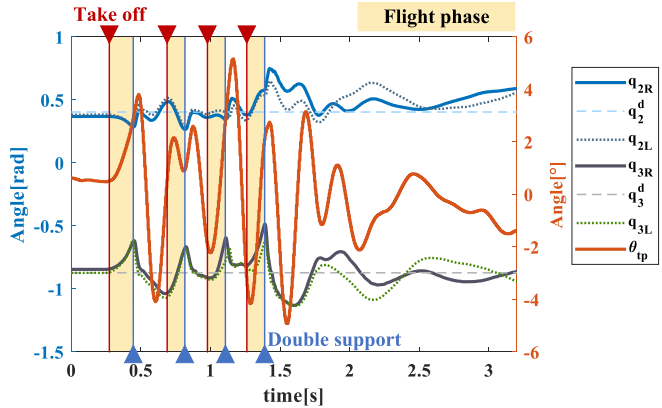


Fig. 13. Variations of the angles of the hip and knee joints of the legs and the angle of the trunk while descending the steps. The yellow shaded area exhibits the flight phase.

periods where one or both wheels are off the ground. BHR-WI with CBCF can absorb the continuous shock of the ground to ensure a stable posture and quickly adjust the desired contact force to prevent falls.

B. Continuous Step-Down Experiment

Fig. 12 demonstrates the whole process of the continuous step-down test. After falling to the ground, BHR-WI can stop steadily. Fig. 13 illustrates the changes in hip and knee joints' angles and trunk pitch angle. The moments of taking off and re-touching the ground when descending the steps are marked. The yellow shaded area represents the taking-off phase while descending the steps. It can be seen that the maximum compression of the hip joint is 21.76° , the maximum angle change is 27.58° , the maximum compression of the knee joint is 15.04° , and the maximum angle change is 36.57° .

Fig. 14 presents the variation of the output torque of the leg joints and wheels during the step-down process. The plotted results indicate that the maximum output torque of the hip joint is 46.36 Nm and the maximum output torque of the knee joint is 77.68 Nm. The maximum wheel output torque is 33.57 Nm.

In this process of going down the steps, the BHR-WI relies only on the movement of the legs to control the posture and absorb the impact, and it relies on the rotation of the wheels to achieve balance control. Currently, we have not added arm control. The carried-out tests exhibit the excellent compliance and robustness of the CBCF.

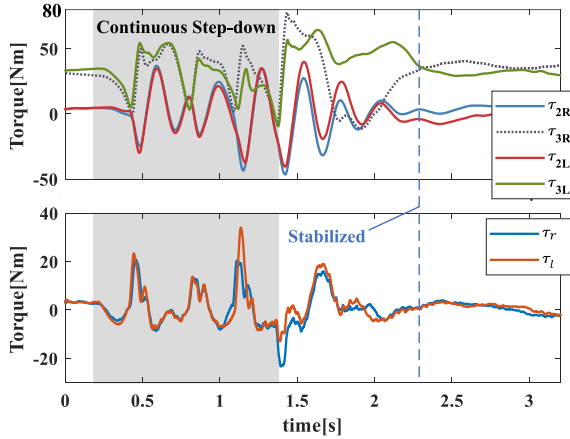


Fig. 14. BHR-WI joint output torque (note: The upper graph presents the changes in the torque of the knee and hip joints during the step-down, and the lower graph shows the changes in the output torque of the wheels). The gray shaded area represents the continuous step-down process.

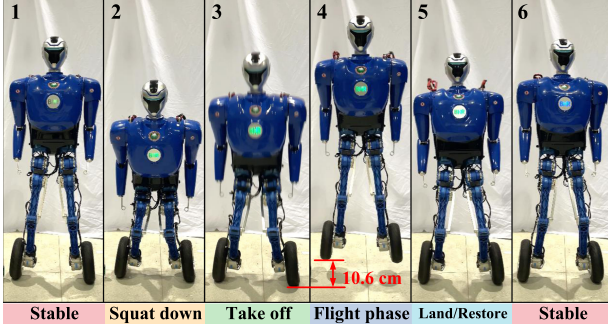


Fig. 15. Different phases of the BHR-WI jump (note: During the flight phase, we do not plan the movement of the legs such as folding the legs).

C. Jumping and Stable Landing

In order to further explore the effectiveness and robustness of the framework, we performed the robot jump test. For convenience, we directly planned the robot's leg movements. When taking off, the robot's CoM is planned to move along the z -direction to achieve a vertical jump. Since the leg movement will cause changes in the angular momentum of the robot during takeoff, we roughly compensate for the change in angular momentum by planning the trunk trajectory (as shown in Fig. 18), and then achieve a stable takeoff.

In planning the trajectory of the CoM during the take-off phase, we define the initial height of the CoM in z -direction is $z_0 = 1.25$ m, and the minimum squat height is set as $z_s = 0.82$ m. When taking off, the time for the CoM to return from z_s to z_0 is set as 0.33 s, so that the BHR-WI has a vertical velocity to take off. As demonstrated in Fig. 15, the vertical jump of BHR-WI is obviously detectable, and the actual measured height from the ground is 10.6 cm.

Fig. 16 illustrates the changes in the angle and output torque of the hip and knee joints during jumping. During the course of landing, the maximum angular compression of the hip joint is 3.48° , and the knee joint is 24.36° . In the takeoff phase, the maximum output torques of the hip joint and the knee joint in

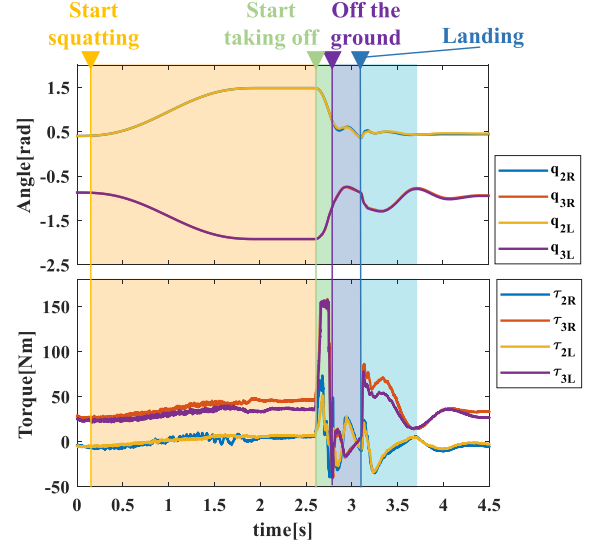


Fig. 16. Upper graph presents the changes in the angles of hip and knee joints during the jump, and the lower graph shows the changes in the output torques of hip and knee joints. Different shaded colors represent different phases of the jump in Fig. 15.

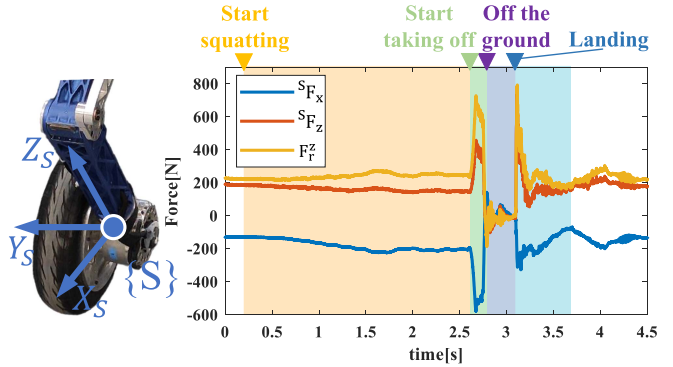


Fig. 17. Left: Coordinate definition of force/torque sensor. Right: Changes in the actual contact force between the right wheel and the ground during take-off and landing.

order are 73.44 Nm and 156 Nm. During the phase of landing, the maximum output torque of the hip joint is obtained as 21.21 Nm and that of the knee joint is 85.67 Nm.

Fig. 17 illustrates the changes in the actual contact force between the right wheel and the ground during takeoff and landing. $S F_x$ and $S F_z$, respectively, denote the forces in the x -direction and z -direction measured by the force/torque sensor. F_r^z represents the value of the vertical contact force of the right wheel (indicated in frame $\{0\}$). During the motion, the maximum value of F_r^z is 792.4 N, which occurs during the landing stage. The maximum values of $S F_x$ and $S F_z$ are -579.1 N and 756.9 N, respectively.

Fig. 18 shows the change of pitch angle of trunk in jumping experiment. According to the demonstrated curve, it can be understood that after the robot lands, the maximum angle of the trunk that deviates from the stable position would be 9.05° . With the CBCF, the robot can absorb the landing impact and restore its balance and stability in about 1.5 s.

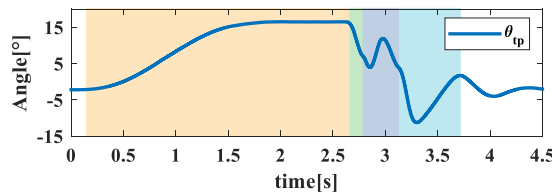


Fig. 18. Changes of trunk pitch angle during takeoff and landing. During the takeoff phase, we roughly plan the trajectory of the trunk to compensate for the change in angular momentum.

V. CONCLUSION

This article proposes a new CBCF for the electrically driven wheel-legged humanoid robot BHR-WI. This framework represents a combination of multidimensional virtual force control of body posture and balance control based on the model prediction to absorb ground impact on rough terrains, resist external disturbance, and maintain a stable posture. It has been verified by experiments that without visual perception, the framework enables the robot to achieve robust motion on rough terrains while exhibiting excellent compliance. After adding the motion of the arms and trunk in the future, the proposed control framework can be more flexible to follow the desired trajectory of CoM through multijoint movement control. The motion of the arms can be used to resist disturbances or balance angular momentum, and the coordinated movement of more joints will contribute to improve body posture and wheel balance control. Moreover, the active control strategy can be added based on the existing controller in the future, so that the robot can give specific responses to different types of terrain and achieve better terrain adaptability.

APPENDIX

The controller designed in this manuscript runs on a computer carried by the robot with a control frequency of 1 kHz. The processor used by the computer is the eighth generation Core i7-8559 U. The communication between the other devices and the computer adopts the EtherCAT industrial Ethernet communication protocol.

In order to perform high dynamic motions such as jumping and moving on rough terrains, the joint modules of BHR-WI require high precision, fast response, and large torque output. We designed integrated joint modules and equipped each joint motor with a planetary reducer with a reduction ratio of 17.43. Low reduction ratios provide the possibility for effective torque control. The specifications of each joint motor are shown in Table I.

In order to obtain the posture information of the robot, we installed an IMU in the chest cavity of BHR-WI. The IMU has 0.2° in roll/pitch and 1° in heading accuracy. Meanwhile, to measure the robot's contact force with the ground, we installed six axis force/torque sensor at the end of the lower leg. The mass of each sensor is 0.36 kg, and the resolution is 1/40000 F.S. The measuring range of the sensor is shown in Table II.

TABLE I
JOINT MOTOR SPECIFICATIONS

Motor Name	Rated Torque [Nm]	Peak Torque [Nm]	Motor Weight [g]	Joint Angle Range [°]
Wheel Motor	2.3	10.7	556	360
Knee Pitch Motor	2.6	11.8	597	0 – 140
Hip Pitch Motor	2.3	10.7	556	-30 – 130
Hip Roll Motor	2.3	10.7	556	-20 – 36
Elbow Pitch Motor	1.9	7.6	364	-120 – 120
Shoulder Pitch Motor	1.2	6.5	320	-150 – 150
Shoulder Roll Motor	1.2	6.5	320	0 – 65

TABLE II
SIX AXIS FORCE/TORQUE SENSOR MEASURING RANGE

	Fx	Fy	Fz	Mx	My	Mz
Measuring Range(N/Nm)	900	900	1800	100	100	100

REFERENCES

- [1] S.-H. Yun, J. Park, J. Seo, and Y.-J. Kim, "Development of an agile omnidirectional mobile robot with GRF compensated wheel-leg mechanisms for human environments," *IEEE Robot. Automat. Lett.*, vol. 6, no. 4, pp. 8301–8308, Oct. 2021.
- [2] H. Peng, J. Wang, S. Wang, W. Shen, D. Shi, and D. Liu, "Coordinated motion control for a wheel-leg robot with speed consensus strategy," *IEEE/ASME Trans. Mechatron.*, vol. 25, no. 3, pp. 1366–1376, Jun. 2020.
- [3] S. Wang, Z. Chen, J. Li, J. Wang, J. Li, and J. Zhao, "Flexible motion framework of the six wheel-legged robot: Experimental results," *IEEE/ASME Trans. Mechatron.*, vol. 27, no. 4, pp. 2246–2257, Aug. 2022.
- [4] G. Lentini et al., "Alter-Ego: A mobile robot with a functionally anthropomorphic upper body designed for physical interaction," *IEEE Robot. Automat. Mag.*, vol. 26, no. 4, pp. 94–107, Dec. 2019.
- [5] J. He, Y. Sun, L. Yang, J. Sun, Y. Xing, and F. Gao, "Design and control of TAWL—a wheel-legged rover with terrain-adaptive wheel speed allocation capability," *IEEE/ASME Trans. Mechatron.*, vol. 27, no. 4, pp. 2212–2223, Aug. 2022.
- [6] Y. Gong et al., "Feedback control of a Cassie bipedal robot: Walking, standing, and riding a segway," in *Proc. Amer. Control Conf.*, 2019, pp. 4559–4566.
- [7] J. Reher, W.-L. Ma, and A. D. Ames, "Dynamic walking with compliance on a cassie bipedal robot," in *Proc. 18th Eur. Control Conf.*, 2019, pp. 2589–2595.
- [8] "Atlas, the next generation," 2016. [Online]. Available: www.youtube.com/watch?v=cNkQT2SUegE
- [9] F. Sygulla and D. Rixen, "A force-control scheme for biped robots to walk over uneven terrain including partial footholds," *Int. J. Adv. Robotic Syst.*, vol. 17, no. 1, 2020, Art. no. 1729881419897472.
- [10] "The humanoid robot Lola walks outside," 2019. [Online]. Available: www.youtube.com/watch?v=cNkQT2SUegE
- [11] L. Han, X. Chen, Z. Yu, X. Zhu, K. Hashimoto, and Q. Huang, "Trajectory-free dynamic locomotion using key trend states for biped robots with point feet," *Inf. Sci.*, vol. 66, 2023, Art. no. 189201.
- [12] L. Wang et al., "Design and dynamic locomotion control of quadruped robot with perception-less terrain adaptation," *Cyborg Bionic Syst.*, vol. 22, 2022, Art. no. 9816495.
- [13] S. Chen, J. Rogers, B. Zhang, and K. Sreenath, "Feedback control for autonomous riding of Hovershoes by a Cassie bipedal robot," in *Proc. IEEE-RAS 19th Int. Conf. Humanoid Robots*, 2019, pp. 1–8.
- [14] "Introducing Handle," 2017. [Online]. Available: www.youtube.com/watch?v=7xvqQeoA8c
- [15] X. Li, H. Yu, H. Feng, S. Zhang, and Y. Fu, "Design and control for WLR-3P: A hydraulic wheel-legged robot," *Cyborg Bionic Syst.*, vol. 4, 2023, Art. no. 0025.
- [16] X. Li, S. Zhang, H. Zhou, H. Feng, and Y. Fu, "Locomotion adaption for hydraulic humanoid wheel-legged robots over rough terrains," *Int. J. Humanoid Robot.*, vol. 18, no. 01, 2021, Art. no. 2150001.
- [17] V. Klemm et al., "Ascento: A two-wheeled jumping robot," in *Proc. Int. Conf. Robot. Automat.*, 2019, pp. 7515–7521.

- [18] V. Klemm et al., "LQR-assisted whole-body control of a wheeled bipedal robot with kinematic loops," *IEEE Robot. Automat. Lett.*, vol. 5, no. 2, pp. 3745–3752, Apr. 2020.
- [19] S. Wang et al., "Balance control of a novel wheel-legged robot: Design and experiments," in *Proc. IEEE Int. Conf. Robot. Automat.*, 2021, pp. 6782–6788.
- [20] J. Zhang et al., "An adaptive approach to whole-body balance control of wheel-bipedal robot Ollie," in *Proc. IEEE/RSJ Int. Conf. Intell. Robots Syst.*, 2022, pp. 12835–12842.
- [21] W. Zhu, F. Raza, and M. Hayashibe, "Reinforcement learning based hierarchical control for path tracking of a wheeled bipedal robot with sim-to-real framework," in *Proc. IEEE/SICE Int. Symp. System Integration*, 2022, pp. 40–46.
- [22] M. Bjelonic, P. K. Sankar, C. D. Bellicoso, H. Vallery, and M. Hutter, "Rolling in the deep-hybrid locomotion for wheeled-legged robots using online trajectory optimization," *IEEE Robot. Automat. Lett.*, vol. 5, no. 2, pp. 3626–3633, Apr. 2020.
- [23] V. S. Medeiros, E. Jelavic, M. Bjelonic, R. Siegwart, M. A. Meggiolaro, and M. Hutter, "Trajectory optimization for wheeled-legged quadrupedal robots driving in challenging terrain," *IEEE Robot. Automat. Lett.*, vol. 5, no. 3, pp. 4172–4179, Jul. 2020.
- [24] E. Vollenweider et al., "Advanced skills through multiple adversarial motion priors in reinforcement learning," in *Proc. IEEE Int. Conf. Robot. Automat.*, 2023, pp. 5120–5126.
- [25] L. Zhao et al., "System design and balance control of a novel electrically-driven wheel-legged humanoid robot," in *Proc. IEEE Int. Conf. Unmanned Syst.*, 2021, pp. 742–747.
- [26] X. Qiu et al., "Upright and crawling locomotion and its transition for a wheel-legged robot," *Micromachines*, vol. 13, no. 8, 2022, Art. no. 1252.
- [27] S. Kajita, F. Kanehiro, K. Kaneko, K. Yokoi, and H. Hirukawa, "The 3D linear inverted pendulum mode: A simple modeling for a biped walking pattern generation," in *Proc. IEEE/RSJ Int. Conf. Intell. Robots Syst. Expanding Societal Role Robot. Next Millennium*, 2001, pp. 239–246.
- [28] C. Liu, J. Ning, and Q. Chen, "Dynamic walking control of humanoid robots combining linear inverted pendulum mode with parameter optimization," *Int. J. Adv. Robotic Syst.*, vol. 15, no. 1, 2018, Art. no. 1729881417749672.
- [29] R. P. M. Chan, K. A. Stol, and C. R. Halkyard, "Review of modelling and control of two-wheeled robots," *Annu. Rev. Control*, vol. 37, no. 1, pp. 89–103, 2013.
- [30] G. Zambella et al., "Dynamic whole-body control of unstable wheeled humanoid robots," *IEEE Robot. Automat. Lett.*, vol. 4, no. 4, pp. 3489–3496, Oct. 2019.
- [31] P. Sardain and G. Bessonnet, "Forces acting on a biped robot. Center of pressure-zero moment point," *IEEE Trans. Syst., Man, Cybern.-Part A: Syst. Humans*, vol. 34, no. 5, pp. 630–637, Sep. 2004.
- [32] S. Ito, H. Asano, and H. Kawasaki, "A balance control in biped double support phase based on center of pressure of ground reaction forces," *IFAC Proc. Volumes*, vol. 36, no. 17, pp. 189–194, 2003.



Zhangguo Yu (Member, IEEE) received the B.S. degree in electronics engineering and the M.S. degree in control engineering from the Southwest University of Science and Technology (SWUST), Mianyang, China, in 1997 and 2005, respectively, and the Ph.D. degree in mechatronics engineering from the Beijing Institute of Technology (BIT), Beijing, China, in 2009.

From 2001 to 2009, he was an Assistant Professor, a Lecturer, and then an Associate Professor with SWUST. He is currently a Professor of mechanical engineering with BIT and also the Director of Intelligent Robotics Institute, BIT. His research interests include motion planning and control of biped robots.



Lianqiang Han received the B.Eng. degree in mechatronic engineering, in 2018, from the Beijing Institute of Technology (BIT), Beijing, China, where he is currently working toward the Ph.D. degree in mechanical engineering with the Intelligent Robotics Institute, School of Mechatronical Engineering.

His research interests include motion planning, balance control, and dynamic working for biped robot with joint torque control.



Xuechao Chen (Member, IEEE) received the B.S. and Ph.D. degrees from the Beijing Institute of Technology (BIT), Beijing, China, in 2007 and 2013, respectively, both in mechatronics engineering.

He was a Visiting Student with the Robotics Institute, Carnegie Mellon University, Pittsburgh, PA, USA, in 2012. He is currently a Professor with the School of Mechatronics Engineering, BIT. His research interests include biped locomotion and dynamics.



Xuejian Qiu received the B.Eng. degree in mechanical engineering from the China Agriculture University (CAU), Beijing, China, in 2020. He is currently working toward the master's degree in mechanical engineering with the Intelligent Robotics Institute, School of Mechatronical Engineering, BIT.

His research interests include motion planning, balance control, and locomotion mode transition control for wheel-legged robot.



Qiang Huang (Fellow, IEEE) received the B.S. and M.S. degrees from the Harbin Institute of Technology, Harbin, China, in 1986 and 1989, respectively, both in electrical engineering, and the Ph.D. degree in mechanical engineering from Waseda University, Tokyo, Japan, in 1996.

From 1996 to 1999, he was a Research Fellow with the National Institute of Advanced Industrial Science and Technology, Tokyo. From 1999 to 2000, he was a Research Fellow with the University of Tokyo, Tokyo. Since 2000, he has been a Professor with the Beijing Institute of Technology (BIT), Beijing, China. He is currently the Executive Director of Beijing Advanced Innovation Center for Intelligent Robots and systems, BIT. His research interests include biped locomotion and biorobotic systems.

Dr. Huang was a recipient of the IFToMM Award of Merit.



Lingxuan Zhao received the B.Eng. degree in vehicle engineering, in 2019, from the Beijing Institute of Technology (BIT), Beijing, China, where he is currently working toward the Ph.D. degree in mechanical engineering with the Intelligent Robotics Institute, School of Mechatronic Engineering.

His research interests include banlance control and dynamic motion control for wheel-legged robot with joint torque control.